



**Abstract**

13  
14  
15  
16  
17  
18  
19  
20  
21  
22  
23  
24  
25  
26  
27

Idealized general circulation models (GCMs) suggest global-mean precipitation ceases to increase with warming in hot climates. However, it is unclear if this occurs in more comprehensive GCMs. Here, we examine precipitation over a wide range of climates simulated with comprehensive GCMs. We find that in the Community Atmosphere Model, global-mean precipitation increases approximately linearly with global-mean surface temperatures up to about 330 K, where it peaks at 5 mm day<sup>-1</sup>. Beyond 330 K, global-mean precipitation decreases substantially despite increasing surface temperatures. This occurs because of increased atmospheric shortwave absorption from water vapor, which limits shortwave radiation available for surface evaporation. Precipitation decreases in the tropics and subtropics, but continues to increase in the extratropics due to increased poleward moisture transport. Precipitable water increases everywhere, resulting in longer water-vapor residence times and implying more episodic precipitation. Other GCMs indicate global-mean precipitation might exhibit a smaller maximum rate and begin to decrease at lower surface temperatures.

**Plain Language Summary**

28  
29  
30  
31  
32  
33  
34  
35  
36  
37  
38  
39  
40  
41  
42  
43  
44

Earth's climate has experienced substantial changes over its history, including periods of extremely cold temperatures where most regions contained ice, and periods of extremely warm temperatures where most regions contained no ice. In this study, we explore how precipitation changed in extremely cold and warm climates using a unique set of coupled climate model simulations. We find that global-mean precipitation increases linearly with global-mean surface temperatures up to 330 K, where it peaks and then decreases as surface temperatures further increase. This occurs because in hot climates, global-mean precipitation is almost entirely balanced by absorbed shortwave radiation at the surface. As the climate warms, the atmosphere contains more water vapor, resulting in increased absorption of shortwave radiation within the atmosphere and decreased absorption of shortwave radiation at the surface. This limits the energy available for surface evaporation. We show that other climate models exhibit qualitatively similar behavior but indicate the peak in global-mean precipitation could occur at lower surface temperatures. These results demonstrate the need to better understand Earth's hydrological cycle in hot climates. These results also have large implications for understanding weathering in past climates and the habitability of other Earth-like planets.

## 1 Introduction

Global-mean precipitation is expected to increase at a rate of 1–3 % per degree of warming in response to rising greenhouse-gas concentrations (Allen & Ingram, 2002; Held & Soden, 2006; Vecchi & Soden, 2007; Jeevanjee & Romps, 2018). This relationship, often referred to as Earth’s global hydrological sensitivity, has been found to be remarkably similar across a variety of greenhouse-gas forcing experiments (Stephens & Ellis, 2008; Lambert & Webb, 2008; Andrews & Forster, 2010; Andrews et al., 2010; O’Gorman et al., 2012; Pendergrass & Hartmann, 2014; DeAngelis et al., 2015; Fläschner et al., 2016; Raiter et al., 2023). This implies that global-mean precipitation in past climates, such as the early Eocene or the mid-Pliocene, can be inferred directly from paleoclimate temperature records. For example, it is estimated that early Eocene surface temperatures were 12–15 K warmer than the present-day climate (Caballero & Huber, 2013; Anagnostou et al., 2016; Inglis et al., 2020), which suggests that global-mean precipitation would have been 12–45 % larger than today.

While the global hydrological sensitivity is a conceptually convenient metric, there is evidence that it varies as a function of climate state, implying that estimates from climates similar to today may not apply to past climates. For instance, O’Gorman and Schneider (2008) simulated a wide range of climates in an idealized GCM and showed that global-mean precipitation ceases to increase with warming in hot climates. Examination of the surface energy budget showed that in hot climates, global-mean precipitation is entirely balanced by absorbed shortwave radiation at the surface, which in the idealized GCM, is insensitive to warming (O’Gorman & Schneider, 2008). However, the idealized GCM simulations employed a simple gray radiation scheme and contained no land, sea ice, or clouds, leaving questions about the behavior of precipitation in comprehensive GCMs.

More recent work examined precipitation in comprehensive GCMs under various atmospheric carbon dioxide ( $\text{CO}_2$ ) levels and found that the global hydrological sensitivity exhibits weak climate state dependence. Good et al. (2012) used a coupled GCM and found that global-mean precipitation is only slightly less sensitive to warming in warm climates. Raiter et al. (2023) examined a broader suite of coupled GCMs and found that the global hydrological sensitivity changes little under large  $\text{CO}_2$  forcing. However, these studies did not explore extremely high atmospheric  $\text{CO}_2$  concentrations and only simulated a narrow range of Cenozoic Era surface temperatures. Thus, in comprehensive GCMs, it remains unclear whether the global hydrological sensitivity is weaker in hot climates and whether precipitation exhibits significant climate state dependence. Notably, analytical radiative arguments introduced by Jeevanjee and Romps (2018) suggest that in hot climates, precipitation may decrease under warming. Yet, this hypothesis has not been confirmed in comprehensive GCMs, which contain clouds and other processes that can modulate radiative fluxes.

In this study, we examine precipitation over a wide range of climates simulated with comprehensive GCMs. We find that in the Community Atmosphere Model (CAM), global-mean precipitation increases approximately linearly with global-mean surface temperatures up to about 330 K, where it peaks at a rate of approximately  $5 \text{ mm day}^{-1}$ . Beyond 330 K, global-mean precipitation decreases substantially despite increasing global-mean surface temperatures. The decrease in precipitation occurs because in hot climates, Earth’s atmosphere contains more water vapor, resulting in increased absorption of shortwave radiation within the atmosphere and decreased absorption of shortwave radiation at the surface, thereby limiting the energy available for surface evaporation. Other GCMs indicate global-mean precipitation might exhibit a smaller maximum rate and begin to decrease at lower surface temperatures. We also find that extratropical precipitation continues to increase despite decreasing global-mean precipitation because of increased poleward latent energy transport. These results have large implications for understanding Earth’s hydrological cycle across various epochs, spanning from the recent past to the Hadean and Archaean eons, as well as for understanding weathering in past climates, and the habitability of other Earth-like planets.

## 2 Data and methods

### 2.1 Climate model output

We use simulation output from a suite of comprehensive GCMs that have participated in different phases of the Coupled Model Intercomparison Project. The simulations come from different GCMs and span a wide range of surface temperatures, enabling us to explore the impact of model physics on precipitation as a function of climate state.

#### 2.1.1 *Community Atmosphere Model (CAM)*

We use a suite of simulations from CAM4, CAM5, and CAM6, which are state-of-the-art atmospheric models within the Community Earth System Model (CESM; Hurrell et al., 2013; Danabasoglu et al., 2020). CAM4 uses different radiative transfer code (Collins et al., 2006) from CAM5 and CAM6, which both use the rapid radiative transfer model for GCMs (Mlawer et al., 1997). CAM4, CAM5, and CAM6 also differ substantially in their physical parameterizations of convection and clouds, leading to different equilibrium climate sensitivities of 3.1 K, 4.2 K, and 5.3 K, respectively (Zhu & Poulsen, 2020).

Each CAM simulation is performed with a slab-ocean model (SOM) and specified atmospheric CO<sub>2</sub> concentration. The framework is described in more detail by Zhu and Poulsen (2020). In short, CAM6 simulations were carried out with 1×, 2×, and 4× the preindustrial CO<sub>2</sub> concentration (284.7 ppmv); CAM5 simulations were carried out with 1×, 2×, 4×, and 8× CO<sub>2</sub>; and CAM4 simulations were carried out with 1×, 2×, 4×, 8×, 16×, 32× and 64× CO<sub>2</sub>. With CAM4, we perform two additional simulations (128× and 256× CO<sub>2</sub>) not described by Zhu and Poulsen (2020). Note that model instability for CAM6 with 8×CO<sub>2</sub> and CAM5 with 16×CO<sub>2</sub> prevented higher CO<sub>2</sub> simulations. Each set of SOM simulations employ identical non-CO<sub>2</sub> preindustrial boundary conditions and mixed layer depths and heat transport convergence derived from corresponding fully coupled preindustrial simulations with a dynamical ocean. All CAM4 and CAM5 simulations were run with a horizontal resolution of 1.9° × 2.5° (latitude × longitude) for 60 model years, except for the CAM4 64×, 128×, and 256×CO<sub>2</sub> simulations, which were run for 80 model years. All CAM6 simulations were run for 80 model years. The last 20 years of each simulation were used to calculate climatologies. The global-mean surface temperature range covered by these simulations is broadly comparable to paleoclimate temperatures over the Cenozoic Era and beyond.

We also use a suite of climate simulations that are described in more detail by Wolf et al. (2018). These simulations use a modified version of CAM4 with a SOM and a horizontal resolution of 4° × 5°. The modified version of CAM4 uses a correlated-k radiative transfer model to accurately simulate extremely warm climates (Wolf & Toon, 2013). We use 22 simulations with atmospheric CO<sub>2</sub> concentrations starting from 1.40625 ppmv and doubling until 2,949,120 ppmv.

#### 2.1.2 *LongRunMIP*

We use a set of simulations from LongRunMIP (Rugenstein et al., 2019), which is a model intercomparison project that aims to better understand centennial and millennial time scale atmosphere–ocean processes in comprehensive, coupled GCMs. We use all GCMs that provide a preindustrial control simulation and 2×, 4×, 8×, and 16× CO<sub>2</sub>. There are no simulations with higher CO<sub>2</sub> forcing. We assume that each preindustrial control simulation has an atmospheric CO<sub>2</sub> concentration of 284.7 ppmv. For all simulations, except those from CNRM-CM6-1, we average each variable over years 970–1,000. For the CNRM-CM6-1 simulations, we average over years 720–750 as this is the longest available time period after 2×CO<sub>2</sub>. Most simulations have little-to-no global-mean ocean heat uptake and are therefore close to equilibrium at this time period.

## 2.2 Energy budget diagnostics

### 2.2.1 Global

Global-mean precipitation can be examined through the surface energy budget. The global-mean (denoted by an overbar) surface energy budget can be expressed as

$$0 = \bar{S} - \bar{L} - L_v \bar{E} - \bar{H} - \bar{G}, \quad (1)$$

where  $S$  is the net downward shortwave flux,  $L$  is the net upward longwave flux,  $E$  is the surface evaporation flux,  $L_v$  is the latent heat of vaporization,  $H$  is the sensible heat flux from the surface into the atmosphere, and  $G$  is ocean heat uptake and storage. On interannual and longer timescales,  $\bar{E}$  is equal to precipitation  $\bar{P}$ , which results in

$$\bar{P} \equiv \bar{E} = \frac{1}{L_v} (\bar{S} - \bar{L} - \bar{H} - \bar{G}). \quad (2)$$

The radiative fluxes  $S$  and  $L$  can be further decomposed into clear-sky (clr) and cloud components (cld) such that  $S = S_{\text{clr}} + S_{\text{cld}}$  and  $L = L_{\text{clr}} + L_{\text{cld}}$ . For the CAM simulations, we decompose  $S$  and  $L$  into clear-sky and cloud components, while for the LongRunMIP simulations, we cannot decompose  $S$  and  $L$  due to the lack of clear-sky surface flux output.

O’Gorman and Schneider (2008) showed that Eq. (2) can explain the structure of global-mean precipitation as a function of climate state, including the processes controlling the maximum rate of precipitation in hot climates.

### 2.2.2 Regional

Regional precipitation can also be examined through the surface energy budget with the addition of the latent energy flux divergence  $\nabla \cdot F_{\text{latent}}$ . On long time scales,

$$P - E = -\frac{1}{L_v} \nabla \cdot F_{\text{latent}}, \quad (3)$$

which means that, using the surface energy budget, regional precipitation can be expressed as

$$P = \frac{1}{L_v} (S - L - H - G - \nabla \cdot F_{\text{latent}}). \quad (4)$$

We examine regional precipitation through the surface energy budget as it connects directly to our approach for global-mean precipitation and provides a physically intuitive understanding of energetic constraints on evaporation, which is how moisture enters the atmosphere. Note that integrating Eq. (4) globally results in exactly Eq. (2). Global and regional precipitation can also be examined through the atmospheric energy budget (e.g., Muller & O’Gorman, 2011; O’Gorman et al., 2012; Pendergrass & Hartmann, 2014; Bonan, Feldl, et al., 2023).

## 3 Precipitation over a wide range of climates

### 3.1 Global-mean precipitation

We begin by examining global-mean precipitation as a function of atmospheric CO<sub>2</sub> concentration and global-mean surface temperature (Fig. 1). Under high CO<sub>2</sub> concentrations, GCMs exhibit large intermodel differences in global-mean surface temperatures (Fig. 1a). For example, across GCMs, global-mean surface temperatures for CO<sub>2</sub> concentrations near 1,000 ppmv range from 289 K to 300 K. While the intermodel spread in surface temperatures is large, these simulations, with the exception of CAM4 (blue and red lines, Fig. 1a), only span a small range of Cenezoic Era paleoclimate temperatures. The two versions of CAM4 with different radiation schemes simulate an even larger range of global-mean surface temperatures, ranging from 265 K to 380 K (blue and red lines, Fig. 1a). Note these

182 simulations indicate that Earth’s climate sensitivity exhibits considerable state dependence  
 183 for global-mean surface temperatures around 310 K, which has been noted in several other  
 184 studies (e.g., Caballero & Huber, 2013; Wolf et al., 2018; Zhu & Poulsen, 2020; Seeley &  
 185 Jeevanjee, 2021; Henry et al., 2023).

186 GCMs also exhibit a large intermodel spread in global-mean precipitation as a function of  
 187 atmospheric CO<sub>2</sub> concentration (Fig. 1b). For example, across GCMs, global-mean precipi-  
 188 tation for CO<sub>2</sub> concentrations near 1,000 ppmv ranges from approximately 2.8 mm day<sup>-1</sup> to  
 189 approximately 4.0 mm day<sup>-1</sup>. Interestingly, for CO<sub>2</sub> concentrations beyond 30,000 ppmv,  
 190 the CAM4 simulations indicate that global-mean precipitation decreases (Fig. 1b) despite  
 191 surface temperature increases (Fig. 1a). Both versions of CAM4 exhibit a global-mean  
 192 precipitation decrease, despite having different radiation codes (blue and red lines, Fig. 1b).

193 These results can be further understood by plotting global-mean precipitation as a function  
 194 of global-mean surface temperature; the derivative of this function is the global hydrological  
 195 sensitivity (Fig. 1c). From cold ( $\sim 270$  K) to warm ( $\sim 320$  K) climates, global-mean precipi-  
 196 tation exhibits a fairly linear relationship with global-mean surface temperature, with only  
 197 slight decreases in the rate of global-mean precipitation increase. In hot ( $> 320$  K) climates,  
 198 the CAM4 simulations indicate that global-mean precipitation increases more slowly with  
 199 global-mean surface temperature and eventually decreases at approximately 330 K (Fig.  
 200 1c). In the CAM4 simulation with the more accurate radiation code, global-mean precipi-  
 201 tation continues to decrease substantially despite increasing surface temperatures. Note  
 202 that other GCMs, such as MPI-ESM1.2 and HadCM3L, exhibit overall weaker increases in  
 203 precipitation for the same surface temperature range as the CAM simulations (gold and  
 204 light blue lines, Fig. 1c).

205 To understand the mechanisms contributing to global-mean precipitation as a function of  
 206 global-mean surface temperature, we examine the surface energy budget (see Section 2.2.1).  
 207 Figure 2 shows the components of the surface energy budget (converted from W m<sup>-2</sup> to mm  
 208 day<sup>-1</sup>). The clear-sky and cloud components of the net surface shortwave and net surface  
 209 longwave fluxes are shown in Figure S1.

210 From cold to warm climates, the global-mean net surface shortwave flux exhibits relatively  
 211 little change, though there is large intermodel spread (Fig. 2a). For example, the CAM  
 212 simulations exhibit little change in the net surface shortwave flux, whereas MPI-ESM1.2  
 213 exhibits a strong decrease. From cold to warm climates, both the net surface longwave flux  
 214 and surface sensible heat flux approach zero with little intermodel spread (Fig. 2b and 2c).  
 215 The net surface longwave flux change is almost entirely driven by the clear-sky component  
 216 (Fig. S1).

217 In hot climates, the net surface longwave flux and surface sensible heat flux are zero or  
 218 slightly positive (Fig. 2b, 2c). This occurs because differences in surface and tropospheric air  
 219 temperatures become small, and the atmosphere approaches the optically thick limit, where  
 220 upward longwave emission at the surface and the downward longwave emission from within  
 221 the atmosphere that reaches the surface occur at almost the same temperature (O’Gorman  
 222 & Schneider, 2008). As a result, global-mean evaporation, and thus global-mean precipita-  
 223 tion, is almost entirely balanced by the net surface shortwave flux, which exhibits a strong  
 224 decrease in hot climates (Fig. 2a). The clear-sky component of the net surface shortwave  
 225 flux decreases in hot climates (Fig. S1) because of increased shortwave absorption by the  
 226 atmosphere due to water vapor (Fig. S2). The decrease in net surface shortwave flux occurs  
 227 in both CAM4 simulations, though the decrease is stronger at high temperatures in the  
 228 CAM4 simulations with the more accurate radiation code (blue and red lines, Fig. 2a).

### 229 3.2 Zonal-mean precipitation

230 We now examine zonal-mean precipitation as a function of global-mean surface temperature  
 231 (Fig. 3). We focus on the CAM simulations to understand the regions contributing to the

232 decrease in global-mean precipitation for surface temperatures beyond 330 K. The same  
 233 analysis for each simulation from LongRunMIP is shown in Figure S3.

234 From cold to warm climates, precipitation increases in most regions, with substantial in-  
 235 creases in the tropics and extratropics and small decreases in the subtropics (Fig. 3a). In  
 236 hot climates ( $> 320$  K), subtropical and tropical precipitation decreases substantially. The  
 237 maximum tropical precipitation is approximately  $10 \text{ mm day}^{-1}$  in warm climates and de-  
 238 creases to approximately  $5 \text{ mm day}^{-1}$  in hot climates. Similarly, subtropical precipitation  
 239 decreases from approximately  $6 \text{ mm day}^{-1}$  in warm climates to approximately  $0 \text{ mm day}^{-1}$   
 240 in hot climates. Notably, from warm to hot climates, despite a decrease in global-mean  
 241 precipitation, precipitation continues to increase in the extratropics, with the polar regions  
 242 experiencing a substantial increase in precipitation (Fig. 3a). Precipitation in the Arctic,  
 243 for instance, increases from approximately  $2 \text{ mm day}^{-1}$  in warm climates to approximately  
 244  $8 \text{ mm day}^{-1}$  in hot climates.

245 To understand the mechanisms contributing to regional precipitation as a function of global-  
 246 mean surface temperature, we examine components of the surface energy budget and latent  
 247 energy flux divergence (see Section 2.2.2). Figures 3b-e show the components of the zonal-  
 248 mean surface energy budget and latent energy flux divergence (converted from  $\text{W m}^{-2}$  to  
 249  $\text{mm day}^{-1}$ ) for the CAM simulations.

250 From cold to warm climates, the net surface shortwave flux remains relatively constant,  
 251 exhibiting weak increases in the polar regions (Fig. 3b). Figure S4 shows the clear-sky and  
 252 cloud components of the zonal-mean net surface shortwave flux and shows that this is related  
 253 mainly to the clear-sky component. The overall increase in zonal-mean precipitation from  
 254 cold to warm climates is contributed mainly by the net surface longwave flux, which becomes  
 255 smaller under warming (Fig. 3c). The surface sensible heat flux contributes weakly to the  
 256 overall increase in zonal-mean precipitation from cold to warm climates (Fig. 3d). The  
 257 latent energy flux divergence contributes most to the zonal-mean pattern of precipitation,  
 258 causing a precipitation increase in the tropics and extratropics, and a precipitation decrease  
 259 in the subtropics (Fig. 3e). Note there are substantial changes in the latent energy flux  
 260 divergence around 320 K that indicate meridional shifts in tropical rainfall, expansion of  
 261 the subtropics, and poleward shifts of the midlatitude stormtracks.

262 In hot climates ( $> 320$  K), the net surface longwave flux and surface sensible heat flux  
 263 become much smaller and approach zero (Fig. 3c, 3d). As a result, in hot climates, regional  
 264 precipitation is almost entirely balanced by the net surface shortwave flux and latent energy  
 265 flux divergence (Fig. 3b, 3e). In the subtropics, the weak export of moisture associated  
 266 with increased poleward latent energy transport (Fig. 3e) is balanced almost entirely by the  
 267 net surface shortwave flux, resulting in no precipitation (Fig. 3a). Note that the subtropics  
 268 continue to see drying in extremely hot climates, largely due to the increased latent energy  
 269 transport (Fig. 3e). In the extratropics, precipitation continues to increase in hot climates  
 270 because of increased poleward latent energy transport. In the polar regions, the decrease  
 271 in net surface shortwave flux is small (Fig. 3b), but the increase in poleward latent energy  
 272 transport is large (Fig. 3e), resulting in an overall precipitation increase (Fig. 3a).

### 273 **3.3 Total precipitable water and precipitation intensity**

274 The decrease in global-mean precipitation for surface temperatures above 330 K has impor-  
 275 tant implications for precipitation intensity and precipitation extremes. Scaling arguments  
 276 and simulations suggest that precipitation extremes depend primarily on the atmospheric  
 277 water vapor content (O’Gorman & Schneider, 2009; O’Gorman & Schneider, 2009), which  
 278 should continue to increase with warming (O’Gorman & Schneider, 2008). A decrease in  
 279 global-mean precipitation but increase in global-mean atmospheric water vapor content im-  
 280 plies that precipitation would have to become more episodic and potentially more intense.

281 Due to the lack of high-frequency temporal output, we are unable to quantitatively examine  
 282 precipitation extremes (e.g., O’Gorman & Schneider, 2009; O’Gorman & Schneider, 2009).  
 283 However, we can examine the total precipitable water and calculate the water vapor resi-  
 284 dence time, defined as the global-mean total precipitable water divided by the global-mean  
 285 precipitation (Trenberth, 1998; Bosilovich et al., 2005). The water vapor residence time can  
 286 help indicate precipitation intensity. For instance, a climate with the same mean precipi-  
 287 tation as today but a longer water vapor residence time implies there is more episodic and  
 288 intense precipitation.

289 The global-mean total precipitable water (Fig. 4a) and global-mean water vapor residence  
 290 time (Fig. 4b) increase with increasing global-mean surface temperatures. From cold to  
 291 warm climates, total precipitable water increases at a rate of 6–7 % K<sup>-1</sup> and the water  
 292 vapor residence time increases at a rate of 4–5 % K<sup>-1</sup>. In hot climates, the total precipitable  
 293 water continues to increase (Fig. 4a), resulting in a global-mean water vapor residence time  
 294 of approximately one year at 350 K (Fig. 4b). The total precipitable water increases  
 295 most in the tropics and subtropics (Fig. 4c), which likely results in regional variations of  
 296 precipitation intensity. For climates between 320–330 K, precipitation is likely more intense  
 297 and episodic due to the relatively similar global-mean precipitation (Fig. 1c) but increase  
 298 in water vapor residence time (Fig. 4b).

#### 299 4 Discussion and conclusions

300 In this study, we examined precipitation over a wide range of climates simulated with com-  
 301 prehensive GCMs. Building on earlier work by O’Gorman and Schneider (2008), we showed  
 302 that global-mean precipitation increases approximately linearly with global-mean surface  
 303 temperatures from cold to warm climates and begins to increase more slowly in hot climates  
 304 (Fig. 1c)—consistent with Good et al. (2012). However, in contrast to these studies, we  
 305 found that global-mean precipitation decreases substantially after 330 K, despite increasing  
 306 surface temperatures (Fig. 1c). This occurs because global-mean precipitation is almost  
 307 entirely balanced by the absorbed shortwave radiation at the surface in hot climates (Fig.  
 308 2). As the climate warms, Earth’s atmosphere contains more water vapor, resulting in in-  
 309 creased absorption of shortwave radiation within the atmosphere and decreased absorption  
 310 of shortwave radiation at the surface (Fig. 2a and Fig. S2). This limits the energy avail-  
 311 able for surface evaporation and causes a decrease in global-mean precipitation with further  
 312 warming. The results confirm the analytical radiative arguments of Jeevanjee and Romps  
 313 (2018) but in comprehensive GCMs with cloud radiative processes.

314 The decrease in global-mean precipitation for surface temperatures beyond 330 K is driven  
 315 by a decrease in tropical and subtropical precipitation (Fig. 3a). Extratropical precipitation  
 316 continues to increase, despite a decrease in global-mean precipitation (Fig. 3a). This occurs  
 317 because of increases in poleward latent energy transport (Fig. 3e), which is a well-known  
 318 feature of hot climates (Caballero & Langen, 2005; O’Gorman & Schneider, 2008). However,  
 319 the increase in poleward latent energy transport exhibits significant deviations from the  
 320 increase expected solely from the Clausius-Clapeyron relation (Held & Soden, 2006). These  
 321 deviations include meridional shifts in tropical rainfall, expansions and contractions of the  
 322 subtropical regions, and poleward migrations of the extratropical storm tracks. A series  
 323 of studies have shown that a one-dimensional moist energy balance model can accurately  
 324 simulate poleward moisture transport in comprehensive GCMs (Siler et al., 2018; Armour et  
 325 al., 2019; Bonan, Siler, et al., 2023; Bonan et al., 2024), suggesting that downgradient energy  
 326 transport might explain the range of poleward latent transport seen in CAM4, including  
 327 dynamical changes associated with the Hadley circulations.

328 While our results show considerable climate state dependence in precipitation, the simu-  
 329 lations used are driven purely by changes in atmospheric CO<sub>2</sub> concentrations and do not  
 330 contain changes in other boundary conditions that impact hot climates (see review by Zhu et  
 331 al., 2024). For example, the early Eocene experienced significant changes in orbital dynam-



332 ics (Lourens et al., 2005) as well as in continental land configurations and ocean circulation  
333 (Barron, 1987; Shellito et al., 2009; Green & Huber, 2013), each of which could potentially  
334 alter the surface energy budget. Examining the effect of other forcings on precipitation in  
335 hot climates might change these results.

336 Despite this caveat, our work has implications for other aspects of Earth’s hydrological  
337 cycle. We showed that global-mean total precipitable water increases more strongly with  
338 warming when compared to global-mean precipitation (Fig. 4a and Fig. 1c), which results  
339 in a longer global-mean water vapor residence time (Fig. 4b). Thus, precipitation would  
340 have to become more episodic at high surface temperatures. However, due to the lack  
341 of higher-frequency output we are unable to quantitatively examine precipitation intensity  
342 and precipitation extremes. Note that recent work showed precipitation in hot climates is  
343 indeed more episodic and occurs in short and intense outbursts separated by multi-day dry  
344 spells (Seeley & Wordsworth, 2021; Dagan et al., 2023). However, these studies employed  
345 an idealized cloud-resolving model with limited domains. It remains unclear what episodic  
346 precipitation looks like in hot climates simulated with comprehensive GCMs. Future work  
347 should explore other characteristics of precipitation in hot climates. Such work will help to  
348 better understand mechanisms for hydrological change in past and future climates.

349 Overall, our results show that precipitation is strongly dependent on the climate state. While  
350 the CAM simulations indicate that global-mean precipitation exhibits a maximum rate of  
351 approximately  $5 \text{ mm day}^{-1}$  and decreasing rates for surface temperatures beyond 330 K,  
352 other GCMs, like HadCM3L and MPI-ESM1.2, indicate that global-mean precipitation  
353 might exhibit a smaller maximum rate and begin to decrease at lower surface temperatures.  
354 These differences are attributable to shortwave radiation and may be related to water vapor  
355 absorption parameterizations in comprehensive GCMs (e.g., Yang et al., 2016). Hence, there  
356 is a need to examine Earth’s hydrological cycle in hot climates simulated with a broader suite  
357 of comprehensive GCMs. Such work will have large implications for understanding various  
358 climate epochs, spanning from the recent past to the Hadean and Archaean eons, as well  
359 as for understanding weathering in past climates, and the habitability of other Earth-like  
360 planets.

### 361 **Acknowledgments**

362 The authors thank Thorsten Mauritsen for helpful comments during early stages of this  
363 research. D.B.B was supported the National Science Foundation (NSF) Graduate Research  
364 Fellowship Program (NSF Grant DGE1745301). This material is based upon work sup-  
365 ported by the National Center for Atmospheric Research (NCAR), which is a major facility  
366 sponsored by the NSF under Cooperative Agreement 1852977.

### 367 **Data Availability Statement**

368 CAM4, CAM5, and CAM6 output is available in the Zenodo repository (<https://doi.org/10.5281/zenodo.3695929>). LongRunMIP output is freely available at <http://www.longrunmip.org/>. The CAM4 output with modified radiation is available at: [https://archive.org/download/EvaluatingClimateSensitivityToCO2AcrossEarthsHistory\\_201809](https://archive.org/download/EvaluatingClimateSensitivityToCO2AcrossEarthsHistory_201809)

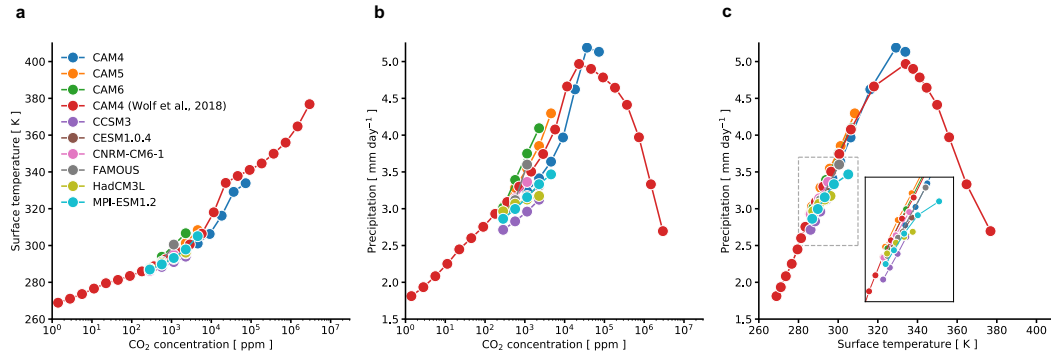


**Figure 1. Global-mean precipitation over a wide range of climates.** (a) Global-mean surface temperature (K) as a function of the atmospheric CO<sub>2</sub> concentration for the CAM slab-ocean model simulations and fully-coupled LongRunMIP simulations. (b) Same as in (a) but for global-mean precipitation (mm day<sup>-1</sup>). (c) Same as in (b) but for global-mean precipitation as a function of global-mean surface temperature. The inset in (c) shows an enlarged version of the grey dashed box.

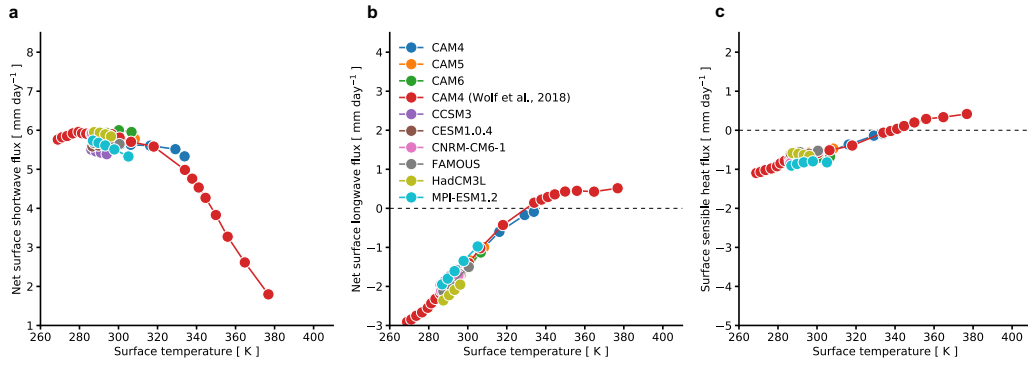


**Figure 2.** Contributions to global-mean precipitation over a wide range of climates.

The global-mean (a) net surface shortwave flux, (b) net surface longwave flux, and (c) surface sensible heat flux as a function of global-mean surface temperature for the CAM slab-ocean model simulations and fully-coupled LongRunMIP simulations. Ocean heat uptake is near-zero for all simulations and is not shown.

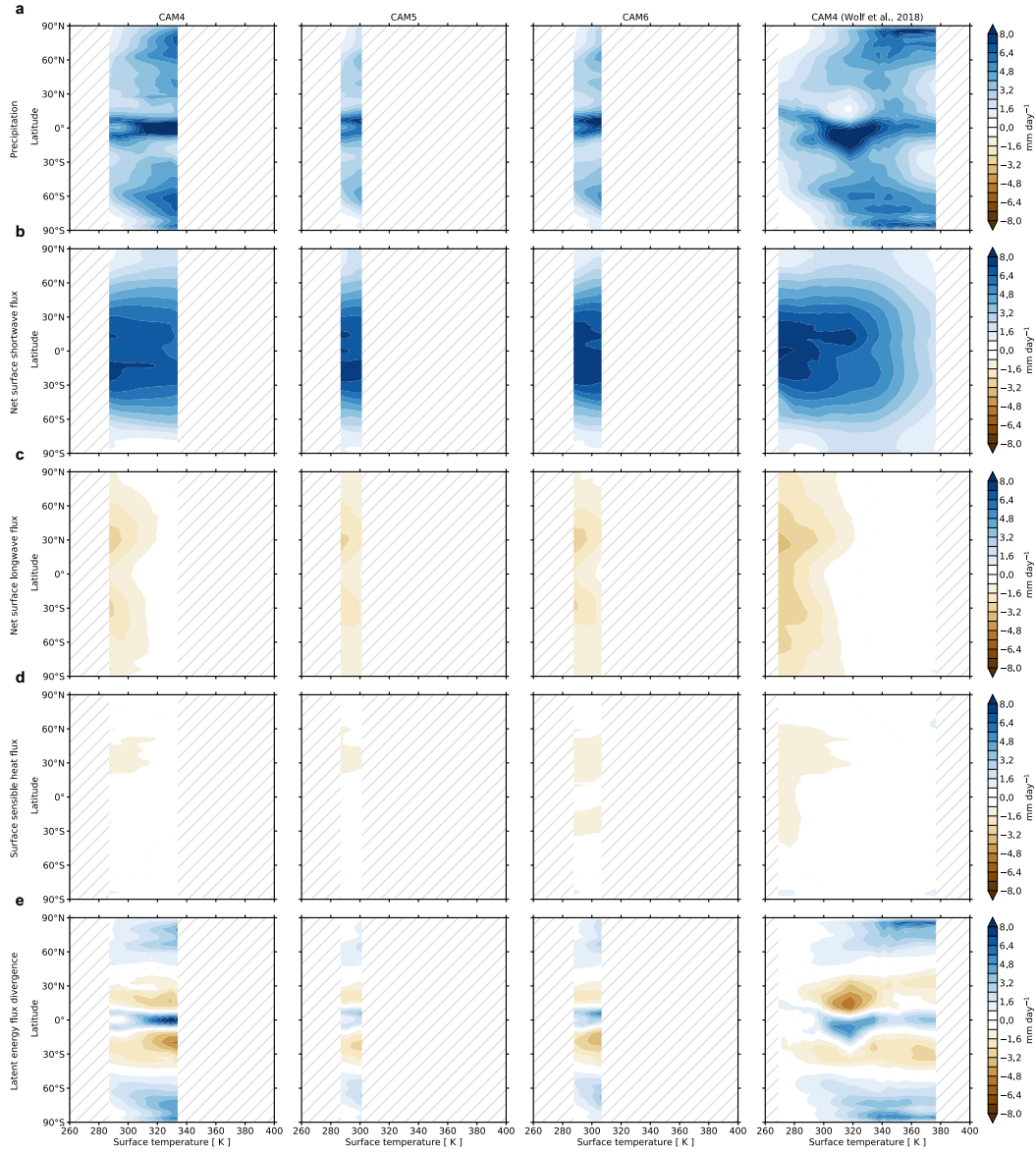


**Figure 3. Zonal-mean precipitation over a wide range of climates.** (a) The zonal-mean precipitation as a function of global-mean surface temperature for the CAM4, CAM5, and CAM6 simulations. The zonal-mean (b) net surface shortwave flux, (c) net surface longwave flux, (d) surface sensible heat flux, and (e) latent energy flux divergence (converted from  $\text{W m}^{-2}$  to  $\text{mm day}^{-1}$ ) as a function of global-mean surface temperature for the CAM4, CAM5, and CAM6 simulations. Ocean heat uptake is zero for all simulations and is not shown. Panels (b-e) add to panel (a). The light grey hatching indicates no simulation data.

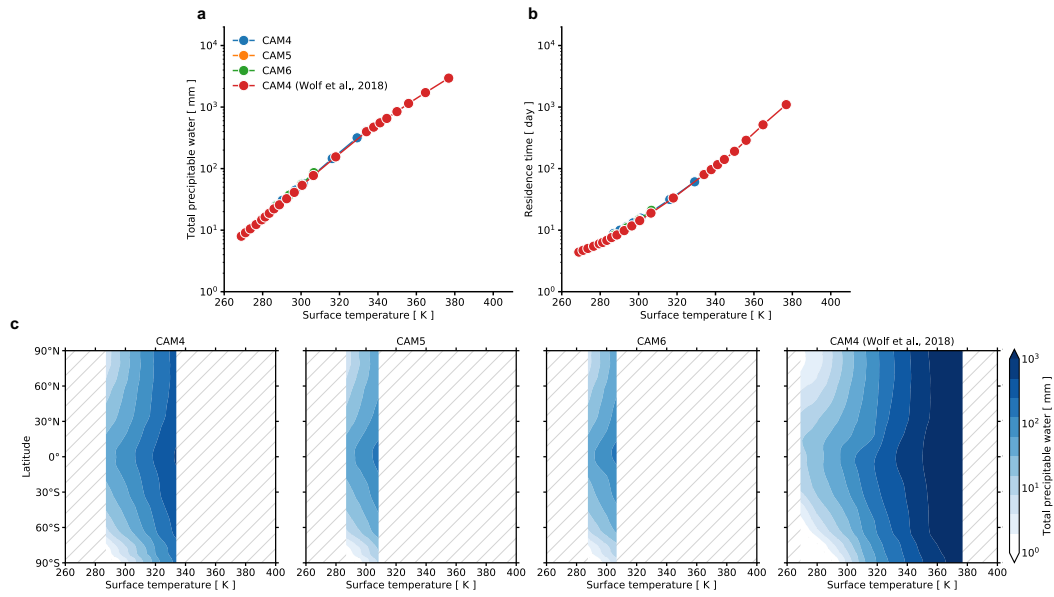


**Figure 4. Residence time of water vapor over a wide range of climates.** The global-mean (a) total precipitable water and (b) residence time of water vapor. The (blue) CAM4, (orange) CAM5, and (green) CAM6 simulations use a slab-ocean model with the Rapid Radiative Transfer Model and the (red) CAM4 simulation uses a slab-ocean model with a more accurate radiation model for high temperatures. (c) Zonal-mean total precipitable water as a function of global-mean surface temperature for the CAM4, CAM5, and CAM6 simulations. The light grey hatching indicates no simulation data.

## References

372

- 373 Allen, M. R., & Ingram, W. J. (2002). Constraints on future changes in climate and the  
374 hydrologic cycle. *Nature*, *419*(6903), 224–232.
- 375 Anagnostou, E., John, E. H., Edgar, K. M., Foster, G. L., Ridgwell, A., Inglis, G. N., ...  
376 Pearson, P. N. (2016). Changing atmospheric CO<sub>2</sub> concentration was the primary  
377 driver of early Cenozoic climate. *Nature*, *533*(7603), 380–384.
- 378 Andrews, T., & Forster, P. M. (2010). The transient response of global-mean precipitation  
379 to increasing carbon dioxide levels. *Environmental Research Letters*, *5*(2), 025212.
- 380 Andrews, T., Forster, P. M., Boucher, O., Bellouin, N., & Jones, A. (2010). Precipitation,  
381 radiative forcing and global temperature change. *Geophysical research letters*, *37*(14).
- 382 Armour, K. C., Siler, N., Donohoe, A., & Roe, G. H. (2019). Meridional atmospheric heat  
383 transport constrained by energetics and mediated by large-scale diffusion. *Journal of*  
384 *Climate*, *32*(12), 3655–3680.
- 385 Barron, E. J. (1987). Eocene equator-to-pole surface ocean temperatures: A significant  
386 climate problem? *Paleoceanography*, *2*(6), 729–739.
- 387 Bonan, D. B., Feldl, N., Siler, N., Kay, J. E., Armour, K. C., Eisenman, I., & Roe, G. H.  
388 (2024). The influence of climate feedbacks on regional hydrological changes under  
389 global warming. *Geophysical Research Letters*, *51*(3), e2023GL106648.
- 390 Bonan, D. B., Feldl, N., Zelinka, M. D., & Hahn, L. C. (2023). Contributions to regional  
391 precipitation change and its polar-amplified pattern under warming. *Environmental*  
392 *Research: Climate*, *2*(3), 035010.
- 393 Bonan, D. B., Siler, N., Roe, G. H., & Armour, K. C. (2023). Energetic constraints on  
394 the pattern of changes to the hydrological cycle under global warming. *Journal of*  
395 *Climate*, *36*(10), 3499–3522.
- 396 Bosilovich, M. G., Schubert, S. D., & Walker, G. K. (2005). Global changes of the water  
397 cycle intensity. *Journal of Climate*, *18*(10), 1591–1608.
- 398 Caballero, R., & Huber, M. (2013). State-dependent climate sensitivity in past warm  
399 climates and its implications for future climate projections. *Proceedings of the National*  
400 *Academy of Sciences*, *110*(35), 14162–14167.
- 401 Caballero, R., & Langen, P. L. (2005). The dynamic range of poleward energy transport in  
402 an atmospheric general circulation model. *Geophysical Research Letters*, *32*(2).
- 403 Collins, W. D., Bitz, C. M., Blackmon, M. L., Bonan, G. B., Bretherton, C. S., Carton,  
404 J. A., ... others (2006). The community climate system model version 3 (CCSM3).  
405 *Journal of Climate*, *19*(11), 2122–2143.
- 406 Dagan, G., Seeley, J. T., & Steiger, N. (2023). Convection and Convective-Organization  
407 in Hothouse Climates. *Journal of Advances in Modeling Earth Systems*, *15*(11),  
408 e2023MS003765.
- 409 Danabasoglu, G., Lamarque, J.-F., Bacmeister, J., Bailey, D., DuVivier, A., Edwards, J.,  
410 ... others (2020). The community earth system model version 2 (CESM2). *Journal*  
411 *of Advances in Modeling Earth Systems*, *12*(2), e2019MS001916.
- 412 DeAngelis, A. M., Qu, X., Zelinka, M. D., & Hall, A. (2015). An observational radiative  
413 constraint on hydrologic cycle intensification. *Nature*, *528*(7581), 249–253.
- 414 Fläschner, D., Mauritsen, T., & Stevens, B. (2016). Understanding the intermodel spread  
415 in global-mean hydrological sensitivity. *Journal of Climate*, *29*(2), 801–817.
- 416 Good, P., Ingram, W., Lambert, F. H., Lowe, J. A., Gregory, J. M., Webb, M. J., ...  
417 Wu, P. (2012). A step-response approach for predicting and understanding non-linear  
418 precipitation changes. *Climate Dynamics*, *39*, 2789–2803.
- 419 Green, J., & Huber, M. (2013). Tidal dissipation in the early Eocene and implications for  
420 ocean mixing. *Geophysical Research Letters*, *40*(11), 2707–2713.
- 421 Held, I. M., & Soden, B. J. (2006). Robust responses of the hydrological cycle to global  
422 warming. *Journal of climate*, *19*(21), 5686–5699.
- 423 Henry, M., Vallis, G. K., Lutsko, N. J., Seeley, J. T., & McKim, B. A. (2023). State-  
424 Dependence of the Equilibrium Climate Sensitivity in a Clear-Sky GCM. *Geophysical*  
425 *Research Letters*, *50*(23), e2023GL104413.

- 426 Hurrell, J. W., Holland, M. M., Gent, P. R., Ghan, S., Kay, J. E., Kushner, P. J., ... others  
 427 (2013). The community earth system model: a framework for collaborative research.  
 428 *Bulletin of the American Meteorological Society*, *94*(9), 1339–1360.
- 429 Inglis, G. N., Bragg, F., Burls, N., Evans, D., Foster, G. L., Huber, M., ... others (2020).  
 430 Global mean surface temperature and climate sensitivity of the EECO, PETM and  
 431 latest Paleocene. *Climate of the past Discussions*, *2020*, 1–43.
- 432 Jeevanjee, N., & Romps, D. M. (2018). Mean precipitation change from a deepening  
 433 troposphere. *Proceedings of the National Academy of Sciences*, *115*(45), 11465–11470.
- 434 Lambert, F. H., & Webb, M. J. (2008). Dependency of global mean precipitation on surface  
 435 temperature. *Geophysical Research Letters*, *35*(16).
- 436 Lourens, L. J., Sluijs, A., Kroon, D., Zachos, J. C., Thomas, E., Röhl, U., ... Raffi, I. (2005).  
 437 Astronomical pacing of late Palaeocene to early Eocene global warming events. *Nature*,  
 438 *435*(7045), 1083–1087.
- 439 Mlawer, E. J., Taubman, S. J., Brown, P. D., Iacono, M. J., & Clough, S. A. (1997).  
 440 Radiative transfer for inhomogeneous atmospheres: RRTM, a validated correlated-k  
 441 model for the longwave. *Journal of Geophysical Research: Atmospheres*, *102*(D14),  
 442 16663–16682.
- 443 Muller, C. J., & O’Gorman, P. (2011). An energetic perspective on the regional response  
 444 of precipitation to climate change. *Nature Climate Change*, *1*(5), 266–271.
- 445 O’Gorman, P. A., & Schneider, T. (2009). The physical basis for increases in precipitation  
 446 extremes in simulations of 21st-century climate change. *Proceedings of the National  
 447 Academy of Sciences*, *106*(35), 14773–14777.
- 448 O’Gorman, P. A., Allan, R. P., Byrne, M. P., & Previdi, M. (2012). Energetic constraints  
 449 on precipitation under climate change. *Surveys in geophysics*, *33*, 585–608.
- 450 O’Gorman, P. A., & Schneider, T. (2008). The hydrological cycle over a wide range of  
 451 climates simulated with an idealized GCM. *Journal of Climate*, *21*(15), 3815–3832.
- 452 O’Gorman, P. A., & Schneider, T. (2009). Scaling of precipitation extremes over a wide  
 453 range of climates simulated with an idealized GCM. *Journal of Climate*, *22*(21),  
 454 5676–5685.
- 455 Pendergrass, A. G., & Hartmann, D. L. (2014). The atmospheric energy constraint on  
 456 global-mean precipitation change. *Journal of climate*, *27*(2), 757–768.
- 457 Raiter, D., Polvani, L. M., Mitevski, I., Pendergrass, A. G., & Orbe, C. (2023). Little  
 458 change in apparent hydrological sensitivity at large CO<sub>2</sub> forcing. *Geophysical Research  
 459 Letters*, *50*(18), e2023GL104954.
- 460 Rugenstein, M., Bloch-Johnson, J., Abe-Ouchi, A., Andrews, T., Beyerle, U., Cao, L., ...  
 461 others (2019). LongRunMIP: motivation and design for a large collection of millennial-  
 462 length AOGCM simulations. *Bulletin of the American Meteorological Society*, *100*(12),  
 463 2551–2570.
- 464 Seeley, J. T., & Jeevanjee, N. (2021). H<sub>2</sub>O windows and CO<sub>2</sub> radiator fins: A clear-  
 465 sky explanation for the peak in equilibrium climate sensitivity. *Geophysical Research  
 466 Letters*, *48*(4), e2020GL089609.
- 467 Seeley, J. T., & Wordsworth, R. D. (2021). Episodic deluges in simulated hothouse climates.  
 468 *Nature*, *599*(7883), 74–79.
- 469 Shellito, C. J., Lamarque, J.-F., & Sloan, L. C. (2009). Early Eocene Arctic climate  
 470 sensitivity to pCO<sub>2</sub> and basin geography. *Geophysical Research Letters*, *36*(9).
- 471 Siler, N., Roe, G. H., & Armour, K. C. (2018). Insights into the zonal-mean response of the  
 472 hydrologic cycle to global warming from a diffusive energy balance model. *Journal of  
 473 Climate*, *31*(18), 7481–7493.
- 474 Stephens, G. L., & Ellis, T. D. (2008). Controls of global-mean precipitation increases in  
 475 global warming GCM experiments. *Journal of Climate*, *21*(23), 6141–6155.
- 476 Trenberth, K. E. (1998). Atmospheric moisture residence times and cycling: Implications  
 477 for rainfall rates and climate change. *Climatic change*, *39*, 667–694.
- 478 Vecchi, G. A., & Soden, B. J. (2007). Global warming and the weakening of the tropical  
 479 circulation. *Journal of Climate*, *20*(17), 4316–4340.

- 480 Wolf, E., Haqq-Misra, J., & Toon, O. (2018). Evaluating climate sensitivity to CO<sub>2</sub> across  
481 Earth's history. *Journal of Geophysical Research: Atmospheres*, *123*(21), 11–861.
- 482 Wolf, E., & Toon, O. (2013). Hospitable Archean climates simulated by a general circulation  
483 model. *Astrobiology*, *13*(7), 656–673.
- 484 Yang, J., Leconte, J., Wolf, E. T., Goldblatt, C., Feldl, N., Merlis, T., ... others (2016).  
485 Differences in water vapor radiative transfer among 1D models can significantly affect  
486 the inner edge of the habitable zone. *The Astrophysical Journal*, *826*(2), 222.
- 487 Zhu, J., & Poulsen, C. J. (2020). On the increase of climate sensitivity and cloud feedback  
488 with warming in the community atmosphere models. *Geophysical Research Letters*,  
489 *47*(18), e2020GL089143.
- 490 Zhu, J., Poulsen, C. J., & Otto-Bliesner, B. L. (2024). Modeling Past Hothouse Climates  
491 as a Means for Assessing Earth System Models and Improving the Understanding of  
492 Warm Climates. *Annual Review of Earth and Planetary Sciences*, *52*.